



HAL
open science

Mineral replacement rate of olivine by chrysotile and brucite under high alkaline conditions

Romain Lafay, German Montes-Hernandez, Emilie Janots, Rodica Chiriac,
Nathaniel Findling, François Toche

► **To cite this version:**

Romain Lafay, German Montes-Hernandez, Emilie Janots, Rodica Chiriac, Nathaniel Findling, et al..
Mineral replacement rate of olivine by chrysotile and brucite under high alkaline conditions. *Journal
of Crystal Growth*, 2012, 347 (1), pp.62-72. 10.1016/j.jcrysgro.2012.02.040 . insu-00719186

HAL Id: insu-00719186

<https://insu.hal.science/insu-00719186>

Submitted on 19 Jul 2012

HAL is a multi-disciplinary open access archive for the deposit and dissemination of scientific research documents, whether they are published or not. The documents may come from teaching and research institutions in France or abroad, or from public or private research centers.

L'archive ouverte pluridisciplinaire **HAL**, est destinée au dépôt et à la diffusion de documents scientifiques de niveau recherche, publiés ou non, émanant des établissements d'enseignement et de recherche français ou étrangers, des laboratoires publics ou privés.

1 **Mineral replacement rate of olivine by chrysotile and brucite under high**
2 **alkaline conditions**

3
4 Romain Lafay^{1*}, German Montes-Hernandez^{1*}, Emilie Janots¹, Rodica Chiriac², Nathaniel
5 Findling¹, Francois Toche²

6
7 ¹ Institut des Sciences de la Terre (ISTerre), UJF-CNRS, F-38041, Grenoble I, Cedex 9,
8 France

9 ² Université Lyon 1, Laboratoire des Multimatériaux et Interfaces UMR CNRS 5615, 43 bd
10 du 11 novembre 1918, 69622 Villeurbanne Cedex, France

11
12
13 * Corresponding authors: Romain Lafay (romain.lafay@ujf-grenoble.fr) and G. Montes-
14 Hernandez (german.montes-hernandez@obs.ujf-grenoble.fr)

16 **Abstract**

17 Olivine mineral replacement by serpentine is one major alteration reaction of oceanic
18 hydrothermalism. In the present experimental study, olivine grains were replaced by
19 chrysotile and brucite under high alkaline conditions. In our study, olivine replacement
20 implied a spatial and temporal coupling of dissolution and precipitation reactions at the
21 interface between olivine and chrysotile-brucite minerals. Coupled dissolution-precipitation
22 led to the alteration of starting olivine grains (so-called primary or parent mineral) to a porous
23 mineral assemblage of chrysotile and brucite with preservation of the initial olivine
24 morphology. This mineral replacement reaction of olivine (serpentinization) has been
25 characterized using XRD, FESEM and FTIR measurements. Moreover, a simple and novel
26 method is here proposed to quantify the mineral replacement rate (or serpentinization rate) of
27 olivine by using thermogravimetric (TG) and differential TG (DTG) analyses.
28 Serpentinization extent depends on the grain size: it is complete after 30 days of reaction for
29 the smallest olivine grains (<30 μm), after 90 days of reaction for the intermediate olivine
30 grains (30 μm -56 μm) and reaches 55% of olivine replacement after 90 days for the largest
31 fraction (56-150 μm). Based on the fitting of the serpentinization extent (ξ_t) versus time (t)
32 by using a kinetic pseudo-second-order model, the serpentinization rates vary from $3.6 \times 10^{-6} \text{ s}^{-1}$
33 ¹ to $1.4 \times 10^{-7} \text{ s}^{-1}$ depending on the olivine grain size. An additional correlation between FTIR
34 spectra analysis and TG measurements is proposed. The mineral replacement reactions
35 frequently observed in natural alteration processes could be a powerful synthesis route to
36 design new porous and/or nanostructured materials.

37 *Keywords:* A1. Serpentinization; A1. Mineral replacement rate; B1. Alkaline medium; B2.
38 Chrysotile nanotubes; A1. TG analyses

39

40 **1 Introduction**

41 Serpentine minerals (chrysotile, lizardite and antigorite) are widespread in Earth
42 oceanic lithosphere and are frequently found in chondrites and other extraterrestrial objects.
43 Serpentine mineralization is of great interest in several fields of research. Serpentinized rocks
44 present a great enrichment in trace elements compared to primary mantle rocks [1–6].
45 Serpentine appears as a vector for trace elements between crustal and mantle reservoirs
46 [2,5,7,8]. Experimental studies have tested the influence of major (e.g. Fe, Ni) and/or trace
47 elements (e.g. Li) on the growth of serpentine [9–14]. This kind of synthesis experiments
48 presents a great interest in medical research due to the asbestos toxicity that can be induced by
49 inhalation of magnesium silicates fibers including chrysotile [15–18]. Serpentine minerals are
50 also crucial for sequestration of CO₂ due to its availability and sequestration capacity [19–21].
51 Indeed a lot of studies are looking for technologies that could possibly contribute to reduce
52 carbon dioxide emissions. Geological sequestration and ex-situ mineralization of CO₂ using
53 serpentine could be one of the most efficient methods considering the enormous quantity of
54 serpentine on Earth [22].

55 In meteorites, serpentine minerals are directly linked to aqueous alteration processes and
56 reaction conditions (e.g. [23] and references therein). In the oceanic lithosphere, serpentines
57 result from interaction between mantle rocks (peridotite composed by olivine and pyroxenes)
58 and hydrothermal fluids, generally with high fracturation dynamic [24,25]. Olivine alters
59 along grain boundaries and fractures to produce a mesh texture that preserves the original
60 olivine morphology at the grain scale [26,27]. This olivine replacement by serpentine is best
61 explained by coupled dissolution-precipitation processes [28–30]. This reequilibration process
62 leads to the replacement of one pristine mineral by a secondary mineral (or assemblage) with
63 a lower solubility in the fluid. Replacement occurs at the fluid/solid interface maintaining the
64 original external grain shape (pseudomorphism). During alteration, a secondary porosity is

65 commonly produced due to volume difference between pristine and secondary minerals,
66 material loss during dissolution and grain fracturation [24,25]. Secondary porosity enables the
67 fluid to move interstitially towards the reaction front until the complete mineral replacement
68 reaction. In oceanic lithosphere, peridotite replacement, and consequent element redistribution
69 associated with this alteration, is primarily controlled by the physic-chemical conditions of the
70 hydrothermal fluid (Temperature, Pressure, fluid speciation, pH). Fluids escaping from deep
71 sea hydrothermal vents show a large variety of composition and pH, reflecting a large range
72 of possible physic-chemical conditions. Amongst them, alkaline fluids with high pH were
73 collected in some hydrothermal fields (e.g., [31,32]).

74 Numerous experimental studies were conduct to reproduce serpentinization in
75 hydrothermal context [33–40] and explain serpentine growth [41]. Kinetic appears faster
76 under alkaline conditions [40,42] but few recent studies have addressed the role of pH on
77 serpentinization kinetic, particularly in alkaline conditions.

78 In the present experimental study, we have investigated the process and kinetics of
79 olivine serpentinization in alkaline hydrothermal conditions (pH = 13.5, measured at 25°C).
80 Experimental products were characterized using XRD, FESEM and FTIR. The
81 serpentinization rate was determined using a simple and novel method based on
82 thermogravimetric analyses (TGA/DTGA). This demonstrates that serpentinization is much
83 faster under alkaline conditions referring to previous study at comparable conditions
84 [35,36,43] and can lead to total replacement of <30µm olivine in less than 30 days and 90
85 days for 30<particle size<56 µm.

86 **2 Materials and Methods**

87 Millimetric grains of olivine San Carlos (F₀₉₀) were crushed by using a Fritsh
88 Pulverisette 7 micro-crusher. Three classes of grain/particle size (particle size<30µm,
89 30<particle size<56µm and 56<particle size<150µm) were isolated by sieving. The samples

90 were washed three times using high-pure water in order to remove the ultrafine particles that
91 possibly stuck at grain surfaces during crushing step. Optical and electron microscopy was
92 performed to control the initial state/appearance of olivine surfaces.

93 **2.1 Alteration experiments**

94 1.5ml of high alkaline solution (1M of NaOH, pH \approx 13.5 at 25°C) and 100mg of San
95 Carlos olivine at a given class of particle size were placed in a Teflon cell reaction (cap-cell
96 also in Teflon). Cell reaction and cap-cell were previously washed by an acidic treatment
97 followed by washing with high-pure water. This cell reaction was immediately assembled into
98 a steel autoclave without agitation, referred as “static batch reactor” and the closed autoclave
99 was placed in a multi-oven (ten independent-temperature compartments) and heated to 150°C
100 or 200°C ($P_{\text{sat}}\sim 0.5\text{Mpa}$ and $P_{\text{sat}}\sim 1.6\text{Mpa}$). Various olivine-alkaline solution reaction times
101 from 3h to 90 days were considered in order to determine the mineral replacement rate (or
102 serpentinization rate) of olivine at the investigated hydrothermal conditions. Particularly, the
103 effect of initial particle size (three different classes: particle size $<30\mu\text{m}$, $30<$ particle
104 size $<56\mu\text{m}$ and $56<$ particle size $<150\mu\text{m}$) on the serpentinization rate of olivine was tested.
105 All experimental conditions are summarized in table 1.

106 At the end of the experiment, the autoclave was quenched in cold water. This
107 manipulation avoids precipitation during cooling with no perturbation of the reaction
108 products. Then, the autoclave was disassembled and the fluid was collected for pH and major
109 elements concentration (Mg, Fe and Si) measurements (not shown in this study). After all
110 experiments, pH of the experimental fluid is still around 13.5 (measured at 25°C). The solid
111 product was dried directly in the Teflon cell at 80°C for 24h. The dry solid product was
112 recovered for further solid characterizations described below.

113 **2.2 X-Ray diffraction measurements**

114 X-Ray diffraction (XRD) analyses were performed in the ISTerre laboratory. All
115 samples were crushed manually. The powders were carefully placed and manually compacted
116 in borosilicated capillaries of 500 μ m of diameter, this corresponds to about 5 mg of sample.
117 XRD patterns were recorded with a Bruker D8 powder diffractometer equipped with a SolX
118 Si (Li) solid state detector from Baltic Scientific Instruments using CuK α 1-K α 2 radiation and
119 a Göbel mirror. Intensities were recorded for an 2θ interval from 5 to 80° with an 8 s counting
120 time per 0.024° 2θ step for bulk mineralogy determination.

121 **2.3 FESEM observations**

122 Grain size and morphology of the experimental products were characterized using
123 secondary or backscattering electrons. Micro-imaging was obtained using Zeiss Ultra 55 Field
124 emission gun scanning electron microscopy (FESEM). This enables a spatial resolution of
125 approximately 1nm at 15 kV. Samples were dispersed by ultrasonic treatment in absolute
126 ethanol for at least 5mn in order to disaggregate the particles. One or two drops of dispersion
127 were placed onto an aluminium support and coated with a thin film of platinumium for SEM
128 observation.

129 **2.4 Thermogravimetric analyses (TGA)**

130 TGA for experimental solid products were performed with a TGA/SDTA 851° Mettler Toledo
131 instrument under the following conditions: sample mass of about 10 mg, platine crucible of
132 150 μ l with a pinhole, heating rate of 10 °C min⁻¹, and inert N₂ atmosphere of 50 ml min⁻¹.
133 Sample mass loss and associated thermal effects were obtained by TGA/DTGA in a
134 temperature range from 30°C to 1200°C. In order to identify the different mass loss steps, the
135 TGA first derivative (rate of mass loss) was used. TGA apparatus was calibrated in terms of
136 mass and temperature. Calcium oxalate was used for the sample mass calibration. The melting
137 points of three compounds (indium, aluminium and copper) obtained from the DTGA signals

138 were used for the sample temperature calibration. The temperature accuracy of the
139 TGA/SDTA system is about $\pm 0.25^{\circ}\text{C}$. The weighting accuracy is around $0.1\mu\text{g}$, which
140 correspond to 0.01% for a 10mg sample.

141

142 **2.5 FTIR measurements**

143 FTIR measurements (in transmission mode) were performed using an IR microscope
144 Bruker Hyperion 3000. The IR beam was focused through a 15x lens and the typical size of
145 infrared aperture is $50*50\mu\text{m}^2$. The light source is a Global(TM) and the beam splitter is in
146 KBr. The spectra were measured from 700 to 4000 cm^{-1} (4cm^{-1} resolution) with a MCT
147 monodetector cooled by liquid nitrogen.

148 Samples must be thin (less than $100\mu\text{m}$) and flat to avoid absorption band saturation or
149 scattering effects. Sample preparation has involved a careful crushing of samples in mortar
150 and manual compaction of fine crushed particles between two K-Br windows. Five spectra
151 per samples were realized; they were fitted using OPUS software.

152 **3 Results and discussion**

153 **3.1 Serpentinization reaction under alkaline conditions**

154 Secondary minerals were identified by XRD and FESEM (Figs. 1 and 2) and they
155 were quantified by TGA (Fig. 3). Under alkaline conditions, olivine is replaced by chrysotile
156 and brucite, independently on the starting grain size of olivine. No other minerals were
157 detected and/or observed during this alteration reaction.

158 FESEM micro-imaging has revealed a clear evolution of particle size and morphology
159 of crystal faces during serpentinization advancement (Fig. 2). Serpentine nucleation at
160 olivine-alkaline solution interfaces is observable by FESEM after only few hours of reaction
161 when the starting grain size is $<30\mu\text{m}$ (Fig. 2a). These occur as nanosized nodules forming
162 irregular sub-micrometric rods. They are still observed onto olivine surfaces after few days of

163 reaction and a more advanced serpentinization reaction (Fig. 2c). The irregular sub-
 164 micrometric rods were identified as chrysotile and brucite “nucleates” from TGA/DTGA in
 165 the solid product (Fig. 3). While brucite is detected by XRD in the first stages of replacement
 166 (e.g. 3 hours of reaction for <30µm grains), chrysotile was not detected by XRD , possibly
 167 due to its poor crystallinity and/or nanometric size. Chrysotile was detected by XRD after 16h
 168 of reaction for the smallest starting grains (<30µm), however, several days of olivine-fluid
 169 interactions are required when the starting grain size is >30µm (Fig. 1a, b). At advanced
 170 alteration stages, serpentinized samples consist of tubular, conical and cylinder-in-cylinder
 171 chrysotile with nanometric diameter and microsized hexagonal brucite were clearly observed
 172 (Fig. 2e, g, h). Diameter of secondary products depends of the starting material grain size. It
 173 increases from ~50 nm for the <30 µm, to 200-300 nmfor 30-56 µm and 56-150 µm fractions.
 174 Lizardite was not observed. Previous study suggested that lizardite crystallized at lower levels
 175 of supersaturation than chrysotile [44]. Here, we confirm that high alkaline pH favors
 176 chrysotile precipitation [40,42].

177 In natural samples, olivine replacement in mesh texture is commonly described as an
 178 assemblage of serpentine±brucite±magnetite. Typically, the magnetite amount depends on the
 179 Mg# (Mg# = Mg / (Mg +Fe)) in primary olivine. Neither iron oxides (ex. magnetite or
 180 hematite) nor oxyhydroxides (ex. goethite) were observed in our experiments. Semi-
 181 quantitative EDS analyses have revealed that the initial iron contained in olivine was
 182 preferentially incorporated as Fe²⁺ into brucite (Mg#_{brucite}=0.84), and slightly sequestered
 183 into/onto chrysotile (Mg#_{chrysotile}=0.95) compared to starting San-Carlos olivine. In our
 184 conditions a part of Fe³⁺ (not determined) might substitute to Si into the chrysotile. In our
 185 experiments, one general reaction of San Carlos olivine alteration can be written as: follows:



187 with X+Y ~0.05 and Z~0.16

188 This isochemical reaction implies a volume increase of ~25% (see discussion below).

189 On the XRD patterns (Fig. 1), characteristic peaks of chrysotile appear in the first hours
190 or days of reaction, depending on the initial particle size of olivine (Fig. 1a, b). Secondary
191 product growth rate is related to the variation of the crystal size with time. On the XRD
192 patterns the full width at half maximum (FWHM) parameter for specific peaks, corresponding
193 to a crystalline compound, can be directly associated to its coherent domain size when
194 instrumental resolution function (IRF) and strain contribution are known. In our case, the
195 FWHM for the plane (002) of chrysotile was used to obtain an estimation of the chrysotile
196 size variation during the serpentinization process. Here, a decrease of FWHM implies an
197 increase of coherent domain size as specified in the Scherrer equation. The FWHM variation
198 with the reaction time reported in figure 1c shows a fast crystal growth step followed by a
199 slow crystal growth step for chrysotile from 3h to 30 days when starting grain size is <30 μm .
200 Conversely, chrysotile coherent domain varies only moderately from 20 to 90 days for
201 starting grain size > 30 μm (Fig. 1c). In this latter case, two explanations are possible: firstly,
202 a preferential growth of other(s) crystal plane(s) than plane (002) is involved, secondly, a
203 dominant nucleation events promoting an increase of particle number concentration with time
204 during mineral replacement of olivine can occur. FESEM observations support the first
205 assumption because they have revealed a higher radial growth of tubular chrysotile for larger
206 starting grain size (30-56 μm and 56-150 μm) at similar reaction time (Fig. 2f, h).

207 **3.2 Determination of serpentinization rate**

208 The time for complete olivine-to-serpentine transformation or complete
209 serpentinization process depends on the starting grain size. For example, 30 days were
210 required when starting grain size was <30 μm while about 90 days were required for the 30-
211 56 μm fraction (Fig. 1a, b). For 56-150 μm starting grain size, around 55% of mineral
212 replacement was reached after 90 days of experiments.

213 Serpentinization rate of olivine was determined by using a simple and novel method
214 combining TGA and DTGA. TGA/DTGA were performed to quantify the molecular water
215 (adsorbed or confined in pores) and hydroxyl groups (-OH) (incorporated in brucite and
216 chrysotile) as illustrated in figure 3. In general, molecular water (H₂O) adsorbed or confined
217 in pores onto mineral assemblage, was released at moderate temperature (<200°C).
218 Conversely, the brucite and chrysotile minerals were dehydroxylated at higher temperatures.
219 Here, a dehydroxylation peak closed to 370°C was associated to brucite. This peak was
220 shifted towards lower temperature, compared to the dehydroxylation of pure brucite peaking
221 at 430°C. This change of thermal stability was related to a significant incorporated amount of
222 iron (Fe²⁺) into brucite structure as recently claimed by Okamoto et al. [45]. Additionally we
223 observed that weight loss ratio between serpentine and brucite is not constant following
224 reaction advancement. Regarding the chrysotile, it was observed that it starts to be
225 dehydroxylated at about 400°C and it was completely dehydroxylated at approximately 700°C
226 for most of the experiments. In several cases, two typical dehydroxylation episodes were
227 measured at 515 and 600 °C, respectively. We note that the starting dehydroxylation step for
228 chrysotile can be overlapped with residual -OH from dehydroxylation of brucite, possibly
229 producing a slight over-estimation of incorporated -OH into the chrysotile phase. This direct
230 measurement was used to calculate the serpentinization extent (%) at a given reaction time as
231 follows:

$$232 \xi_t = ((-OH)_{\text{measured}} / (-OH)_{\text{theoretical}}) * 100 \quad (2)$$

233 where (-OH)_{theoretical} is the theoretical weigh (in %) of hydroxyl groups incorporated in
234 chrysotile (400°C to 700°C) with a chemical formula simplified to Mg₃Si₂O₅(OH)₄ for the (-
235 OH)_{theoretical} considered. Then, the serpentinization extent was correlated with reaction time (ξ_t
236 vs. t). These experimental-calculated data is displayed in figure 3. As previously stated, a
237 complete serpentinization extent was determined after 30 days for smaller olivine grains

238 (<30 μm) and after 90 days for intermediate olivine grains (30<grain size<56). These results
239 clearly show that the serpentinization rate strongly depends on the starting grain size of
240 olivine. This explains why for larger olivine grains (56<grain size<150 μm), about 55% of
241 serpentinization extent was only reached after 90 days of olivine-fluid interactions.

242 Experimental data reported in figure 4 were fitted by using a kinetic pseudo-second-
243 order model. This simple kinetic model describes a fast serpentinization step followed by a
244 slow serpentinization step until an asymptotic maximum with time. Its integrated form can be
245 expressed as follows:

$$246 \quad \xi_t = \frac{\xi_{\max} t}{t_{1/2} + t} \quad (3)$$

247 where ξ_t , is the serpentinization extent for a given reaction time t , ξ_{\max} , the maximum
248 serpentinization extent (close to 100% for a complete serpentinization) and $t_{1/2}$ the half
249 serpentinization time. The fast serpentinization step can be associated to the fast dissolution of
250 smaller olivine grains initially far from equilibrium, but the dissolution process was spatially
251 and temporally coupled to a fast precipitation of chrysotile and brucite. For this reason, the
252 external shape of starting olivine grains (primary or parent mineral) was preserved, leading to
253 a porous granular material composed of chrysotile and brucite minerals when complete
254 mineral replacement of olivine was reached. Finally, the mineral replacement initial-rate v_0
255 (or serpentinization initial-rate) was defined as the slope of the tangent line when time t tends
256 toward zero on the r vs t curve. Analytically, $v_0 = (\xi_{\max}/t_{1/2})$ and it varies from $3.6 \times 10^{-6} \text{ s}^{-1}$ to
257 $1.4 \times 10^{-7} \text{ s}^{-1}$ respectively for <30 μm grain size and 56-150 μm grain size. Full serpentinization
258 was not obtain experimentally on 56<particle size<150 μm but the theoretical model
259 presented predict a close to complete serpentinization (>90%) around 2 years.

260 Indeed, the fluid/olivine interface depending of the initial olivine grain size is the main factor
261 controlling the initial rate. These kinetic parameters concerning the three different size classes
262 of olivine and respective correlation factors are summarized in table 2.

263 The uncertainties of the TG-method result from the calculation method. The main
264 approximation is the systematic consideration of the same temperature range (400-700°C).
265 Referring to all the experiments, a variation of the temperature range of $\pm 50^\circ\text{C}$ will only
266 induce a difference of 1- 5% for the final serpentinization advancement calculated. Based on
267 this calculation we assure that the maximum uncertainty of the proposed methods is around
268 5% as reported in figure 4. The uncertainty on the calculated initial rate is directly depending
269 on the standard deviation obtained for $t_{1/2}$ and ξ_{max} (Table 2).

270 In a complementary way, the transmission FTIR spectra were obtained. Characteristic
271 stretching bands for hydroxyl group (-OH) in chrysotile-brucite and for Si-O group in olivine-
272 chrysotile were used. Particularly, the relative (-OH)/(Si-O) ratio using integrated bands
273 intensities or maximum band intensities was correlated with the serpentinization extent
274 deduced from TG/DTG analyses (Fig. 5). This gives two calibration curves that can be used to
275 determine serpentinization rate using FTIR measurements. However, FTIR measurements
276 should be taken with caution because of the overlapping of -OH (for brucite and serpentine)
277 and Si-O groups (for serpentine and olivine). We could overcome this problem if
278 serpentine/brucite produced molar ratio stayed constant following reaction time, but as
279 described before it is not the case. Here, we conclude that the TG/DTG analyses are a
280 powerful tool to determine the mineral replacement rate of olivine by chrysotile-brucite
281 mineral assemblage. For this specific case, the FTIR measurements provide a first information
282 about the olivine serpentinization extent.

283 This study confirms that the serpentinization rate is enhanced by high alkaline
284 conditions. Serpentinisation rate has been studied for a large variety of experimental

285 conditions under neutral conditions [33–40,46]. For comparison, serpentinization extent of
286 50-100 μm starting grain size at 200°C reached only ~20% after ~4 months under neutral
287 conditions (Seyfried et al., 2007). This corresponds to a kinetic 5 times slower to our results
288 on the largest starting grain size (56-150 μm).

289 **3.3 Serpentinization steps and reaction mechanism**

290 Contemporaneously, the first steps of reaction in alkaline medium are characterized by
291 a fast dissolution of olivine associated to the formation of preferential dissolution figures as
292 notches and etch pits (Fig. 6a, b, c) [44–46]. Conjointly, precipitation of the first nucleates of
293 brucite and chrysotile occur at the olivine surface. FESEM observations have revealed the
294 preservation of olivine shape after complete serpentinization (Fig. 7). This suggests that
295 olivine alteration invokes coupled dissolution-precipitation processes [28]. Despite ultrasonic
296 treatment and dispersion on ethanol (up to 1h30), which can easily break up the new
297 brucite/chrysotile mineral assemblage, the shape and size of olivine grains are always
298 preserved regardless the completion of the reaction. The few scattered chrysotile grains
299 observed are the result of tearing from olivine grain surfaces and are not the result of
300 precipitation from saturated solution away from olivine grain. Based on these results, we
301 assume a higher super-saturation of solution with respect to chrysotile tubes at the olivine-
302 solution interfaces. Supersaturation at olivine-alkaline solution interfaces allows rapid
303 heterogeneous serpentine nucleation as small nodules of chrysotile and brucite (Fig. 2a). This
304 nucleation phase is followed by a phase of epitaxial growth of chrysotile and brucite forming
305 a porous medium (Fig. 6d, e, f). Chrysotile grows as elongated tubes with various morphology
306 (conical, cylinder in cylinder) with a size depending on starting olivine grain size. Largest
307 starting grain size induces smallest reacting surface and thus slower kinetic of alteration and
308 formation of largest chrysotiles particles. Olivine grain size influenced initial dissolution rate
309 v_0 , passivation state and general kinetic of alteration.

310 Serpentinization reaction is then favored by the formation of notches connected to a
311 micro-fracturing network inside olivine (e.g. 32 days of reaction for >30 μm grains; Fig. 6b,
312 c). This micro-fracturing network might start following ordered families of fine-scale
313 fractures from olivine grains [44]. In the oceanic crust, the microfracturing may be attributed
314 to the stress generated by the volume increase during olivine serpentinization [28]. In our free
315 fluid system, there is no evident expansion during olivine replacement. Volume increase due
316 to olivine serpentinization (25%) is likely accounted by material loss in solution, but it could
317 also cause the microfracturing [28,50]. With the formation of smaller sub-grains,
318 microfracturing allows an easier fluid percolation and increase the total reaction-surface (Fig.
319 6e, f). This process permits a continuous and total replacement of olivine by chrysotile and
320 brucite as summarized in figure 8. This is in agreement with natural observation and
321 development of mesh type texture described in natural rocks [26–28,50–52]. Fluid can
322 percolate everywhere without formation of a passivation layer at grain surface. The formation
323 of a protective layer would induce a non-continuous passivation process by blocking intra-
324 particles diffusion [53]. Mass transfer will play a major role for the preservation of volume
325 and shape of starting olivine grain.

326

327 **4 Conclusion**

328 Olivine alteration was investigated under alkaline conditions for different starting
329 grain sizes at 200 °C. In this study, we were able to follow complete olivine replacement by
330 an assemblage of chrysotile and brucite.

331 Thermogravimetric analyses were used to investigate the dehydroxylation of hydrated
332 phases and thus the serpentinization extent as a function of time. Based on this innovative
333 approach, we were able to estimate punctually the serpentinization advancement and a kinetic

334 pseudo-second-order model was used to describe experimental data. This could allow a
335 prediction of reaction advancement for the largest starting grain size.

336 We also established two calibration curves between the -OH/Si-O bands measured in
337 FTIR and the degree of serpentinization. This enables to have an estimation of the kinetic
338 rates of serpentinization directly from the FTIR spectra analysis. This must be considered
339 with caution because of the overlapping of -OH bands between brucite and serpentine.

340 Under our experimental conditions, olivine is replaced by chrysotile and brucite by
341 coupled dissolution-precipitation processes. Fast dissolution of olivine, preferential
342 dissolution features formation and process of grain subdivisions by fracturing are involved to
343 explain a complete mineral replacement of olivine. This implies the preservation of external
344 shape of olivine grains as typically observed in natural systems.

345

346

347 **Acknowledgements**

348 The authors are grateful to French National Center for Scientific Research (CNRS and
349 University Joseph Fourier (UJF) in Grenoble for providing the financial support. R. Lafay was
350 supported by a Ph.D grant from French education ministry. The authors are grateful to IPAG
351 institute where infrared measurements were performed.

352

353 **References:**

354

355 [1] F. Deschamps, S. Guillot, M. Godard, C. Chauvel, M. Andreani, K. Hattori, In situ
356 characterization of serpentinites from forearc mantle wedges: Timing of serpentinization and
357 behavior of fluid-mobile elements in subduction zones, *Chemical Geology*. 269 (2010) 262–
358 277.

359 [2] K. Hattori, S. Guillot, Volcanic fronts form as a consequence of serpentinite
360 dehydration in the forearc mantle wedge, *Geology*. 31 (2003) 525–528.

361 [3] K. Hattori, S. Guillot, Geochemical character of serpentinites associated with high- to
362 ultrahigh-pressure metamorphic rocks in the Alps, Cuba, and the Himalayas: Recycling of
363 elements in subduction zones, *Geochemistry Geophysics Geosystems*. 8 (2007).

364 [4] C.-T.A. Lee, M. Oka, P. Luffi, A. Agranier, Internal distribution of Li and B in
365 serpentinites from the Feather River Ophiolite, California, based on laser ablation inductively
366 coupled plasma mass spectrometry, *Geochem. Geophys. Geosyst.* 9 (2008) Q12011.

367 [5] T.M. McCollom, E.L. Shock, Fluid-rock interactions in the lower oceanic crust:
368 Thermodynamic models of hydrothermal alteration, *J. Geophys. Res.* 103 (1998) 547–575.

369 [6] F. Vils, L. Pelletier, A. Kalt, O. Müntener, T. Ludwig, The Lithium, Boron and
370 Beryllium content of serpentinized peridotites from ODP Leg 209 (Sites 1272A and 1274A):
371 Implications for lithium and boron budgets of oceanic lithosphere, *Geochimica et*
372 *Cosmochimica Acta*. 72 (2008) 5475–5504.

373 [7] F. Deschamps, S. Guillot, M. Godard, M. Andreani, K. Hattori, Serpentinites act as
374 sponges for Fluid-Mobile-Elements in abyssal and subduction zone environments, *Terra*
375 *Nova*. 23 (2011) 171–178.

376 [8] S. Guillot, K.H. Hattori, J. de Sigoyer, T. Nagler, A.-L. Auzende, Evidence of
377 hydration of the mantle wedge and its role in the exhumation of eclogites, *Earth and Planetary*
378 *Science Letters*. 193 (2001) 115–127.

379 [9] A. Bloise, E. Belluso, E. Fornero, C. Rinaudo, E. Barrese, S. Capella, Influence of
380 synthesis conditions on growth of Ni-doped chrysotile, *Microporous and Mesoporous*
381 *Materials*. 132 (2010) 239–245.

382 [10] A. Bloise, E. Belluso, E. Barrese, D. Miriello, C. Apollaro, Synthesis of Fe-doped
383 chrysotile and characterization of the resulting chrysotile fibers, *Cryst. Res. Technol.* 44
384 (2009) 590–596.

385 [11] A.B. Bloise, Hydrothermal alteration of Ti-doped forsterite to chrysotile and
386 characterization of the resulting chrysotile fibers, *njma*. 185 (2009) 297–304.

387 [12] E. Korytkova, L. Pivovarova, V. Gusarov, Influence of iron on the kinetics of
388 formation of chrysotile nanotubes of composition $(\text{Mg, Fe})_3\text{Si}_2\text{O}_5(\text{OH})_4$ under hydrothermal
389 conditions, *Geochemistry International*. 45 (2007) 825–831.

390 [13] A. McDonald, B. Scott, G. Villemure, Hydrothermal preparation of nanotubular
391 particles of a 1:1 nickel phyllosilicate, *Microporous and Mesoporous Materials*. 120 (2009)
392 263–266.

393 [14] B. Wunder, F. Deschamps, A. Watenphul, S. Guillot, A. Meixner, R. Romer, et al.,
394 The effect of chrysotile nanotubes on the serpentine-fluid Li-isotopic fractionation,
395 *Contributions to Mineralogy and Petrology*. 159 (2010) 781–790.

396 [15] G. Falini, E. Foresti, I.G. Lesci, B. Lunelli, P. Sabatino, N. Roveri, Interaction of
397 Bovine Serum Albumin with Chrysotile: Spectroscopic and Morphological Studies, *Chem.*
398 *Eur. J.* 12 (2006) 1968–1974.

399 [16] A.F. Gualtieri, M.L. Gualtieri, M. Tonelli, In situ ESEM study of the thermal
400 decomposition of chrysotile asbestos in view of safe recycling of the transformation product,
401 *Journal of Hazardous Materials*. 156 (2008) 260–266.

402 [17] E. Foresti, E. Fornero, I.G. Lesci, C. Rinaudo, T. Zuccheri, N. Roveri, Asbestos

- 403 health hazard: A spectroscopic study of synthetic geoinspired Fe-doped chrysotile, *Journal of*
404 *Hazardous Materials*. 167 (2009) 1070–1079.
- 405 [18] P. Sabatino, L. Casella, A. Granata, M. Iafisco, I.G. Lesci, E. Monzani, et al.,
406 Synthetic chrysotile nanocrystals as a reference standard to investigate surface-induced serum
407 albumin structural modifications, *Journal of Colloid and Interface Science*. 314 (2007) 389–
408 397.
- 409 [19] A. Beinlich, H. Austrheim, J. Glodny, M. Erambert, T.B. Andersen, CO₂
410 sequestration and extreme Mg depletion in serpentinized peridotite clasts from the Devonian
411 Solund basin, SW-Norway, *Geochimica et Cosmochimica Acta*. 74 (2010) 6935–6964.
- 412 [20] F. Larachi, I. Daldoul, G. Beaudoin, Fixation of CO₂ by chrysotile in low-pressure
413 dry and moist carbonation: Ex-situ and in-situ characterizations, *Geochimica et*
414 *Cosmochimica Acta*. 74 (2010) 3051–3075.
- 415 [21] T.M. McCollom, J.S. Seewald, A reassessment of the potential for reduction of
416 dissolved CO₂ to hydrocarbons during serpentinization of olivine, *Geochimica et*
417 *Cosmochimica Acta*. 65 (2001) 3769–3778.
- 418 [22] T. Yajima, T. Ohsumi, Y. Mizuochi, A. Ninomiya, T. Kato, - Field study on CO₂
419 fixation by serpentinite rock-bed, dans: *Greenhouse Gas Control Technologies 7*, Elsevier
420 Science Ltd, Oxford, 2005: p. 2027–2030.
- 421 [23] P. Beck, E. Quirico, G. Montes-Hernandez, L. Bonal, J. Bollard, F.-R. Orthous-
422 Daunay, et al., Hydrous mineralogy of CM and CI chondrites from infrared spectroscopy and
423 their relationship with low albedo asteroids, *Geochimica et Cosmochimica Acta*. 74 (2010)
424 4881–4892.
- 425 [24] M. Andreani, A. Baronnet, A.-M. Boullier, J.-P. Gratier, A microstructural study of a
426 « crack-seal » type serpentine vein using SEM and TEM techniques, *European Journal of*
427 *Mineralogy*. 16 (2004) 585–595.
- 428 [25] M. Andreani, C. Mével, A.-M. Boullier, J. Escartin, Dynamic control on serpentine
429 crystallization in veins: Constraints on hydration processes in oceanic peridotites, *Geochem.*
430 *Geophys. Geosyst.* 8 (2007) Q02012.
- 431 [26] F.J. Wicks, E.J.W. Whittaker, Serpentine textures and serpentinization, *Canadian*
432 *Mineralogist*. 15 (1977) 459–488.
- 433 [27] B. Evans, The serpentinite multisystem revisited: Chrysotile is metastable,
434 *international Geology review*. 46 (2004) 479–506.
- 435 [28] A. Putnis, Mineral Replacement Reactions, *Reviews in Mineralogy and*
436 *Geochemistry*. 70 (2009) 87–124.
- 437 [29] A. Putnis, C.V. Putnis, The mechanism of reequilibration of solids in the presence of
438 a fluid phase, *Journal of Solid State Chemistry*. 180 (2007) 1783–1786.
- 439 [30] Putnis A., Mineral replacement reactions: from macroscopic observations to
440 microscopic mechanisms, *Mineralogical Magazine*. 66 (2002) 689–708.
- 441 [31] D.S. Kelley, J.A. Karson, D.K. Blackman, G.L. Früh-Green, D.A. Butterfield, M.D.
442 Lilley, et al., An off-axis hydrothermal vent field near the Mid-Atlantic Ridge at 30[deg] N,
443 *Nature*. 412 (2001) 145–149.
- 444 [32] K.A. Ludwig, D.S. Kelley, D.A. Butterfield, B.K. Nelson, G. Früh-Green, Formation
445 and evolution of carbonate chimneys at the Lost City Hydrothermal Field, *Geochimica et*
446 *Cosmochimica Acta*. 70 (2006) 3625–3645.
- 447 [33] D.E. Allen, W.E. Seyfried, Compositional controls on vent fluids from ultramafic-
448 hosted hydrothermal systems at mid-ocean ridges: An experimental study at 400°C, 500 bars,
449 *Geochimica et Cosmochimica Acta*. 67 (2003) 1531–1542.
- 450 [34] A.H. Macdonald, W.S. Fyfe, Rate of serpentinization in seafloor environments,
451 *Tectonophysics*. 116 (1985) 123–135.
- 452 [35] C. Marcaillou, M. Muñoz, O. Vidal, T. Parra, M. Harfouche, Mineralogical evidence

453 for H₂ degassing during serpentinization at 300 °C/300 bar, *Earth and Planetary Science*
454 *Letters*. 303 (2011) 281–290.

455 [36] B. Martin, W.S. Fyfe, Some experimental and theoretical observations on the kinetics
456 of hydration reactions with particular reference to serpentinization, *Chemical Geology*. 6
457 (1970) 185–202.

458 [37] W.E. Seyfried Jr, W.E. Dibble Jr, Seawater-peridotite interaction at 300°C and 500
459 bars: implications for the origin of oceanic serpentinites, *Geochimica et Cosmochimica Acta*.
460 44 (1980) 309–321.

461 [38] W.E. Seyfried Jr., D.I. Foustoukos, Q. Fu, Redox evolution and mass transfer during
462 serpentinization: An experimental and theoretical study at 200 °C, 500 bar with implications
463 for ultramafic-hosted hydrothermal systems at Mid-Ocean Ridges, *Geochimica et*
464 *Cosmochimica Acta*. 71 (2007) 3872–3886.

465 [39] W.W. Wegner, W.G. Ernst, Experimentally determined hydration and dehydration
466 reaction rates in the system MgO–SiO₂–H₂O, *American Journal of Science*. 283A (1983)
467 151–180.

468 [40] K. Yada, K. Iishi, Growth and microstructure of synthetic chrysotile, *American*
469 *Mineralogist*. 62 (1977) 958–965.

470 [41] A. Baronnet, B. Devouard, Topology and crystal growth of natural chrysotile and
471 polygonal serpentine, *Journal of Crystal Growth*. 166 (1996) 952–960.

472 [42] K. Yada, K. Iishi, Serpentine minerals hydrothermally synthesized and their
473 microstructures, *Journal of Crystal Growth*. 24–25 (1974) 627–630.

474 [43] W.E. Seyfried Jr., D.I. Foustoukos, Q. Fu, Redox evolution and mass transfer during
475 serpentinization: An experimental and theoretical study at 200 °C, 500 bar with implications
476 for ultramafic-hosted hydrothermal systems at Mid-Ocean Ridges, *Geochimica et*
477 *Cosmochimica Acta*. 71 (2007) 3872–3886.

478 [44] C. Normand, A.E. Williams-Jones, R.F. Martin, H. Vali, Hydrothermal alteration of
479 olivine in a flow-through autoclave: Nucleation and growth of serpentine phases, *American*
480 *Mineralogist*. 87 1699–1709.

481 [45] A. Okamoto, Y. Ogasawara, Y. Ogawa, N. Tsuchiya, Progress of hydration reactions
482 in olivine–H₂O and orthopyroxene–H₂O systems at 250 °C and vapor-saturated pressure,
483 *Chemical Geology*. 289 (2011) 245–255.

484 [46] M. Bentabol, M.D. Ruiz Cruz, F.J. Huertas, Hydrothermal synthesis (200°C) of Co-
485 kaolinite and Al-Co-serpentine, *Applied Clay Science*. 42 (2009) 649–656.

486 [47] J. Hövelmann, H. Austrheim, A. Beinlich, I. Anne Munz, Experimental study of the
487 carbonation of partially serpentinized and weathered peridotites, *Geochimica et*
488 *Cosmochimica Acta*. 75 (2011) 6760–6779.

489 [48] A. Awad, A.F. Koster van Groos, S. Guggenheim, Forsteritic olivine: effect of
490 crystallographic direction on dissolution kinetics, *Geochimica et Cosmochimica Acta*. 64
491 (2000) 1765–1772.

492 [49] M.A. Velbel, J.M. Ranck, Etch pits on naturally altered olivine from dunites of the
493 Appalachian Blue Ridge Mountains, North Carolina, USA, *Mineral Mag*. 72 (2008) 145–148.

494 [50] A. Putnis, H. Austrheim, Fluid-induced processes: metasomatism and metamorphism,
495 *Geofluids*. 10 (2010) 254–269.

496 [51] F.J. Wicks, E.J.W. Whittaker, J. Zussman, An idealized model for serpentine textures
497 after olivine, *The Canadian Mineralogist*. 15 (1977) 446–458.

498 [52] J.B. Moody, Serpentinization: a review, *Lithos*. 9 (1976) 125–138.

499 [53] G. Montes-Hernandez, A. Pommerol, F. Renard, P. Beck, E. Quirico, O. Brissaud, In
500 situ kinetic measurements of gas–solid carbonation of Ca(OH)₂ by using an infrared
501 microscope coupled to a reaction cell, *Chemical Engineering Journal*. 161 (2010) 250–256.

502

503

504 **Figure Captions:**

505

506 Table 1: Summary of the experimental conditions.

507

508 Table 2: Summary of kinetic parameters obtained from the pseudo-second-order model.

509

510 Figure 1: XRD patterns following reaction advancement, a) with starting grain size <30 μ m, b)
511 with starting grain size 30-56 μ m, c) example of plot for the peak corresponding to bragg
512 angle (2θ) of 12.1° and miller indice (002) with a gaussian deconvolution and plot of FWHM
513 following reaction time for this peak. O: olivine, B: Brucite and S: serpentine.

514 Figure 2: Scanning electron microscope imaging of the experimental products. All shown
515 experiments have been performed at pH=13.5 (at 25°C) and 200°C, for <30 μ m (a, b, c and
516 e), 30-56 μ m (d, f, g) and 56-150 μ m (h) grains size. a) chrysotile and brucite nodules after
517 3hours of reaction (run no.1), b) chrysotile tube after 30 days of reaction (run 8) and c)
518 nodules aggregated in a tubular shape after 3 days of reaction (run no.5), d) chrysotiles
519 “bunch” at olivine grain surface after 10 days of reaction (run no.13), e) characteristic
520 brucite/chrysotile assemblage after 30 days of reaction (run no.6), f,g) characteristic
521 brucite/chrysotile assemblage and thick cylinder-in cylinder chrysotile after 90 days of
522 reaction (run no.18), and h) characteristic brucite/chrysotile assemblage after 32 days of
523 reaction (run no.20). Bru: brucite, Ctl: chrysotile, Ol: olivine.

524

525 Figure 3: a) Thermogravimetric analyses (TGA) for experiments of 3 hours to 30 days (run
526 no. 1,3,5,6,7and 8) with fraction grains <30 μ m, b) focus and decomposition of TGA and
527 DTG corresponding spectra after 10 days of reaction.

528

529

530 Figure 4: Serpentinization degree versus time for the hydration reaction at different grain sizes
531 for $T=200^{\circ}\text{C}$, $P_{\text{sat}}=1.6\text{Mpa}$ and $\text{fluid/solid}=15$. Maximum error bars corresponding to 5% of
532 the serpentinization extent calculated was also reported. Data were fitted by using a kinetic
533 pseudo-second-order model.

534 Figure 5: a) Transmission spectra (in absorbance) for starting grain size $<30\mu\text{m}$ after 3 hour
535 (run no.1) and 30 days (run no.8) of reaction with corresponding base line and range
536 employed for treatment. Blue area correspond to -OH band integration A1 with maximum
537 intensity I1, green area correspond to Si-O band integration A2 with maximum intensity I2, b)
538 corresponding -OH/Si-O ratio: $A1/A2$ and $I1/I2$ following serpentinization advancement
539 determined by TG and DTG analysis, square, triangle and circles correspond respectively to
540 experiments for $<30\mu\text{m}$, $30-56\mu\text{m}$ and $56-150\mu\text{m}$ starting grain size fraction (empty for
541 $A1/A2$ and black for $I1/I2$) with corresponding standard deviation corresponding, black line
542 correspond to best linear regression with the exclusion of red point.

543 Figure 6: Scanning electron microscope imaging of the experimental products for starting
544 grain size $<30\mu\text{m}$ (a), $30-56\mu\text{m}$ (c-f) and $56-150\mu\text{m}$ (b). a) etch pits at olivine grain surface
545 after 3 days (run no.5), b) dissolution notches after 32 days of reaction (run no. 20), c)
546 dissolution notches after 24 days of reaction (run no. 14), d) chrysotile micro-tubes at olivine
547 grain surface after 3 days of reaction (run no.12), e) contact between two olivine grains and f)
548 microfracturing in section after 10 days of reaction (run no.13). Red dotted lines represent
549 initial border of the supposed crack. Ctl: chrysotile, Ol: olivine.

550 Figure 7: XRD pattern and corresponding scanning electron microphotography from pure
551 starting San Carlos olivine to close to 100% of replacement by serpentine and brucite. Note
552 the preservation of the olivine grains dimension and shape. S: serpentine, B: brucite, O:
553 olivine.

554 Figure 8: Schematic synthesis presenting the different steps of olivine replacement by
555 chrysotile and brucite.

556 Table 1

| Run no. | T (°C) | Time | grain size (µm) | Olivine to Chrysotile conversion (%) | products starting-material |
|---------|--------|--------|-----------------|--------------------------------------|----------------------------|
| 1 | 200 | 3 h | <30 µm | 10.3 | O>C>B |
| 2 | 200 | 16 h | <30 µm | 21.7 | O>C>B |
| 3 | 200 | 24 h | <30 µm | 24.6 | O>C>B |
| 4 | 200 | 48 h | <30 µm | 37.5 | O>C>B |
| 5 | 200 | 72 h | <30 µm | 51.7 | O≈C>B |
| 6 | 200 | 10 day | <30 µm | 73.8 | C>O>B |
| 7 | 200 | 20 day | <30 µm | 88.8 | C>B>O |
| 8 | 200 | 30 day | <30 µm | 98.0 | C>B |
| 9 | 200 | 90 day | <30 µm | 98.2 | C>B |
| 10 | 150 | 30 day | <30 µm | 49.5 | O≈C>B |
| 11 | 150 | 66 day | <30 µm | not determined | C>O>B |
| 12 | 200 | 3day | 30-56 µm | 19.6 | O>C>B |
| 13 | 200 | 10 day | 30-56 µm | 26.2 | O>C>B |
| 14 | 200 | 24 day | 30-56 µm | 46.2 | O≈C>B |
| 15 | 200 | 41 day | 30-56 µm | 77.1 | C>O>B |
| 16 | 200 | 51 day | 30-56 µm | 71.1 | C>O>B |
| 17 | 200 | 72 day | 30-56 µm | 88.9 | C>B>O |
| 18 | 200 | 90 day | 30-56 µm | 94.4 | C>B>O |
| 19 | 200 | 13 day | 56-150 µm | 10.7 | O>C>B |
| 20 | 200 | 32 day | 56-150 µm | 26.6 | O>C>B |
| 21 | 200 | 60 day | 56-150 µm | 44.2 | O>C>B |
| 22 | 200 | 90 day | 56-150 µm | 55.4 | C>O>B |

557 All experiments have been performed at pH 13.5 (measured at 25°C). Saturated pressure is
558 constant: 1.6MPa for 200°C and 0.5 MPa for 150°C reactions. Fluid/rock ratio is always ~15.
559 O: olivine, C: chrysotile, B: brucite.

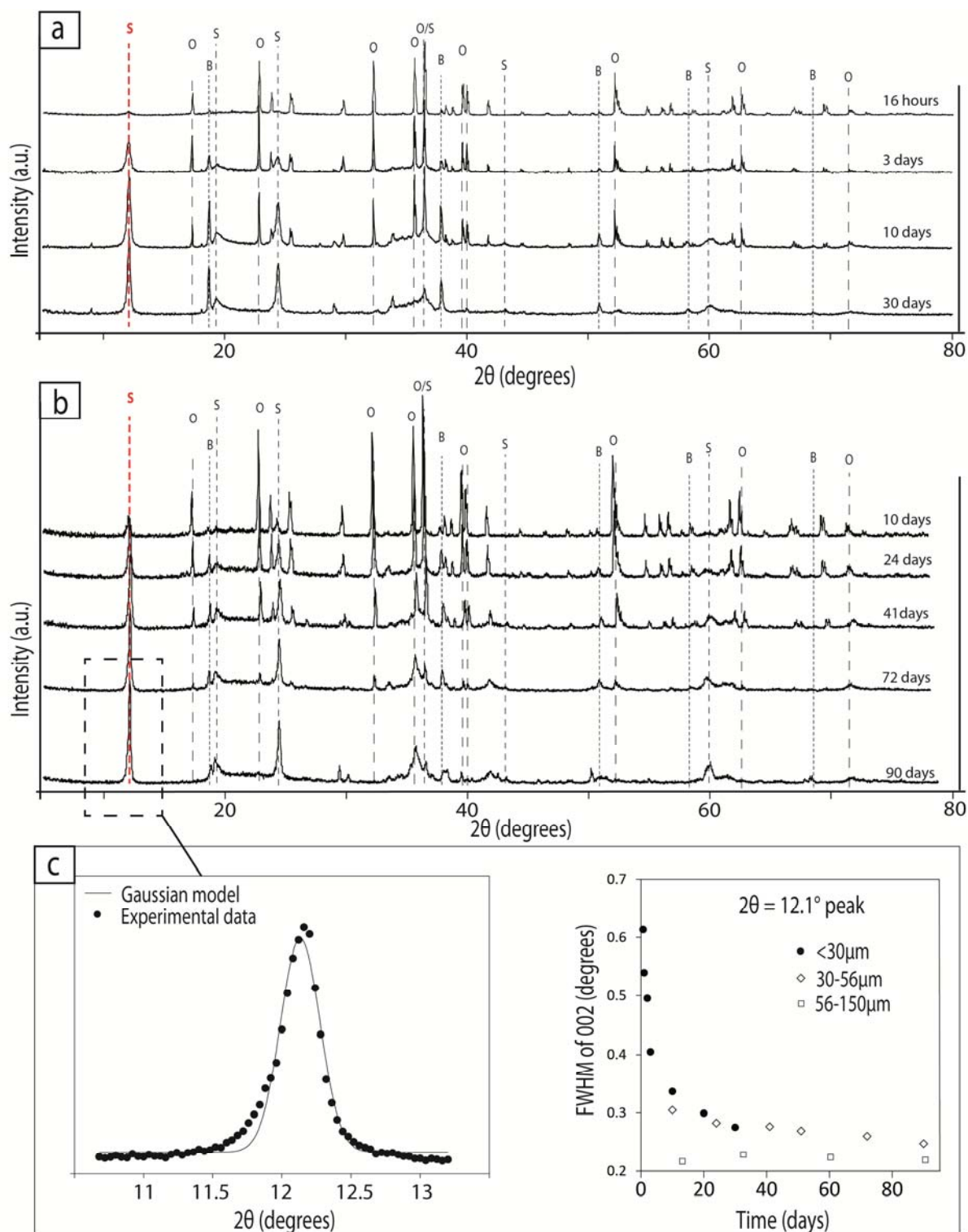
560 Table 2

| Initial particule size of olivine | Smax (%) | | t _½ (days) | Initial rate (1/s) | fitting r ² |
|--------------------------------------|----------|---------|-----------------------|-----------------------|------------------------|
| | Exp. | Calc. | | | |
| <30 μm | 97.96 | 100±1.7 | 3.2±0.3 | 3.62-06±0.35E-06 | 0.989 |
| 30-56 μm | 94.35 | 100±8.5 | 23.1±5.3 | 5.01E-07±0.9E-07 | 0.947 |
| 56-150 μm | 55.4 | 100±16 | 79±21 | 1.46E-07±0.2E-07 | 0.981 |

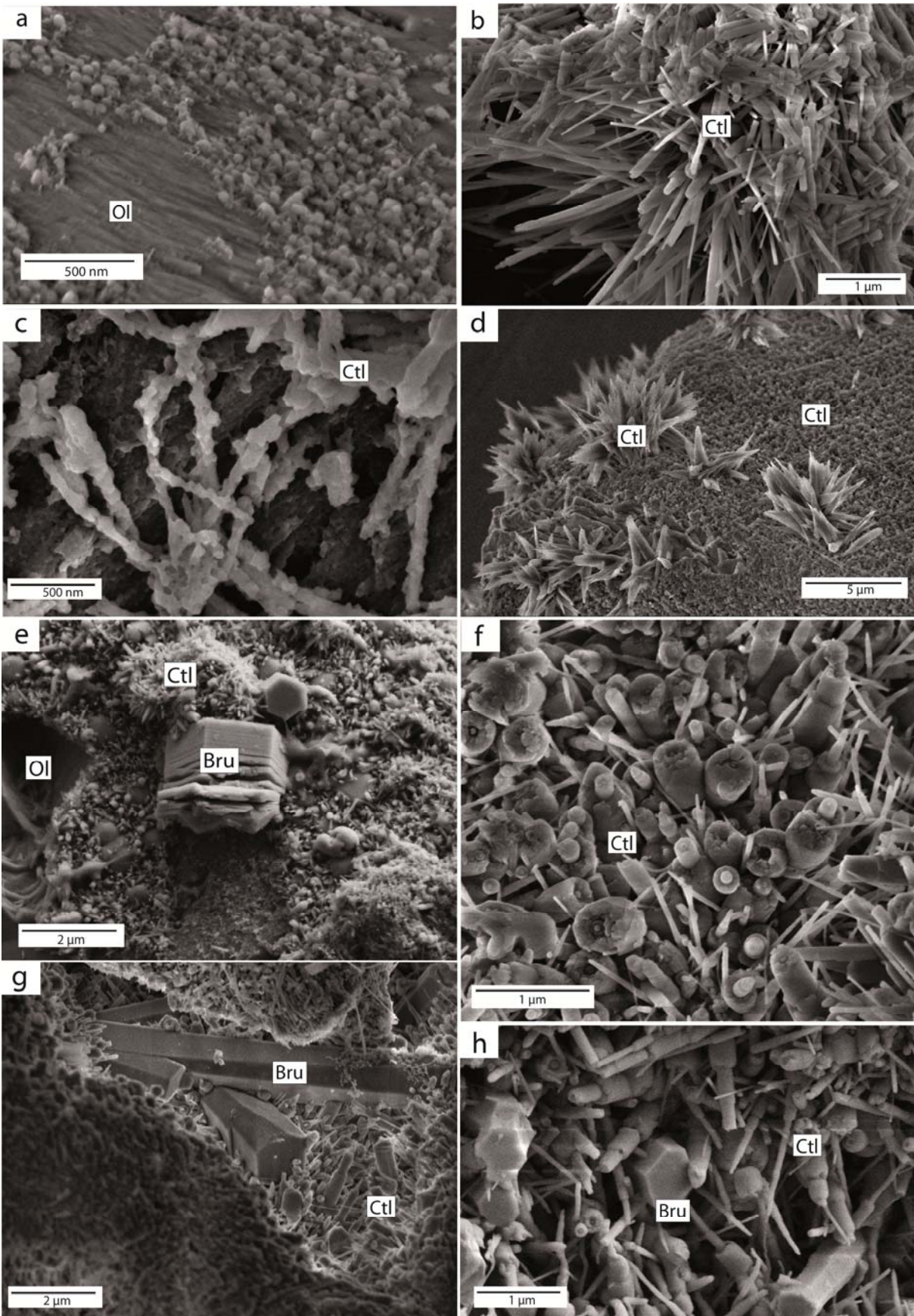
561

562

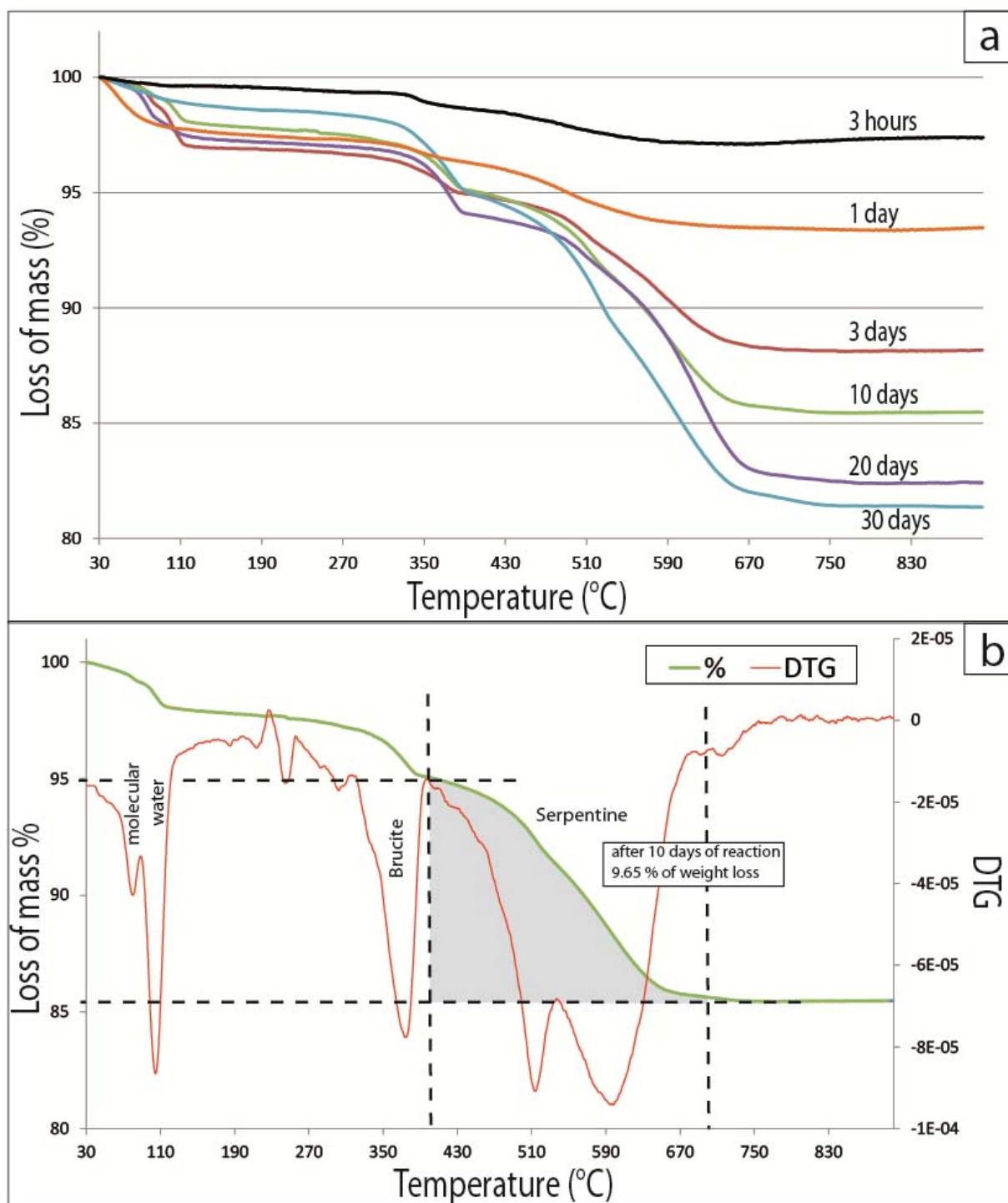
563 Figure 1



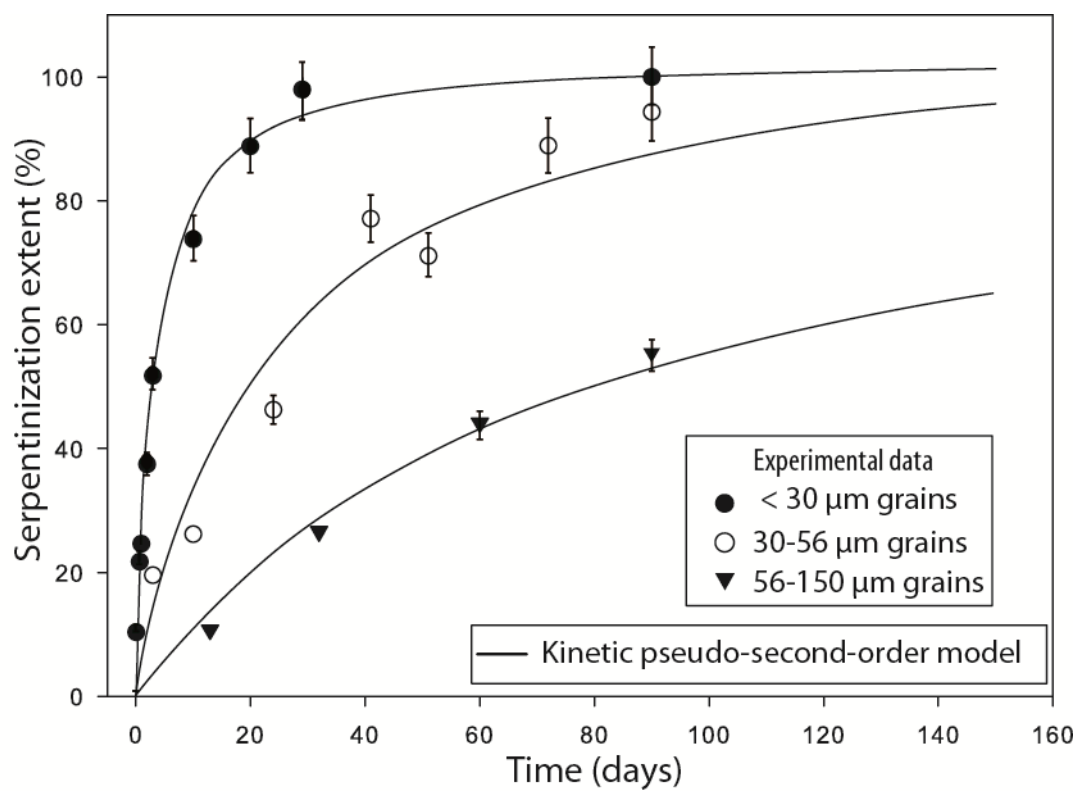
564

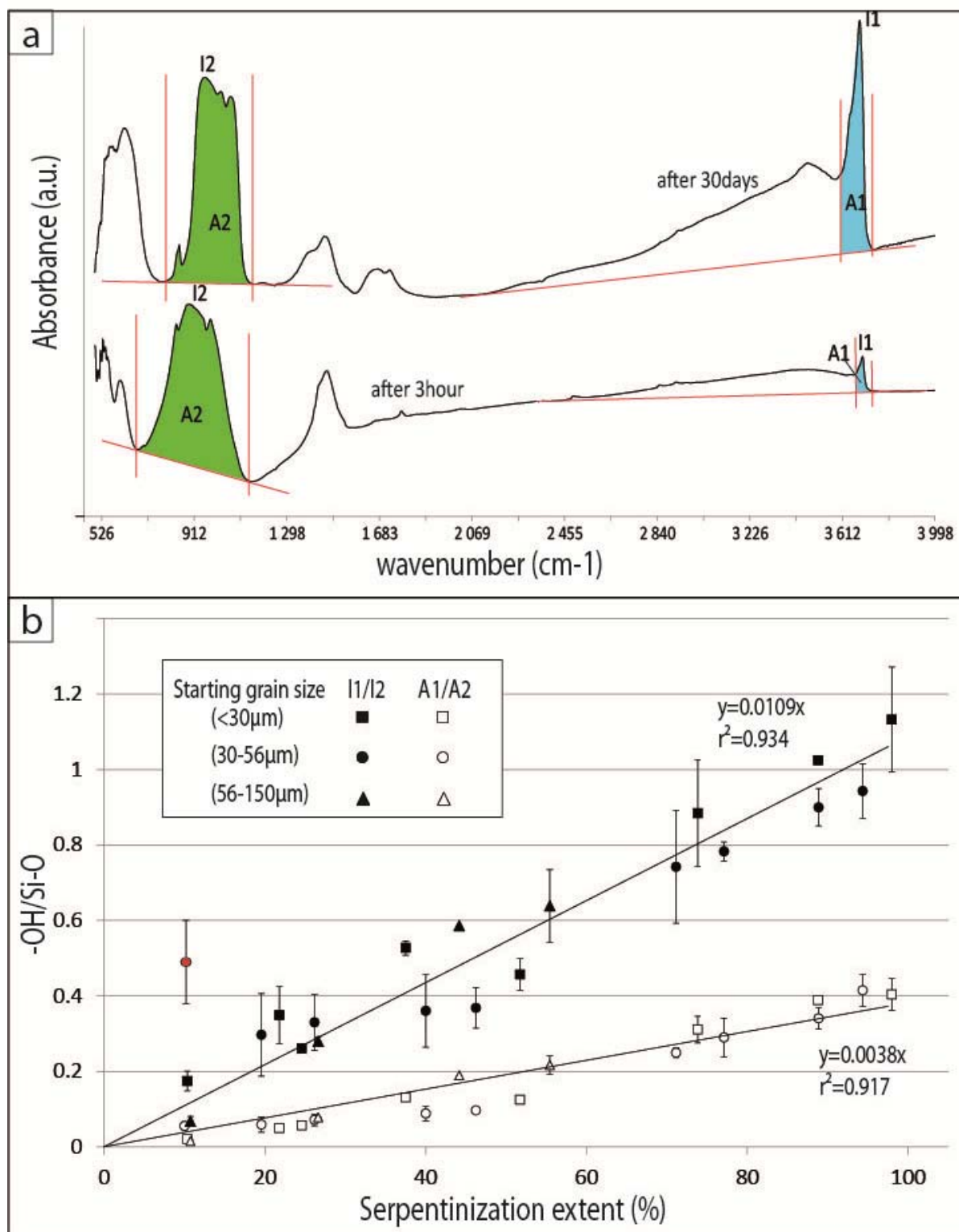


567 Figure 3



568

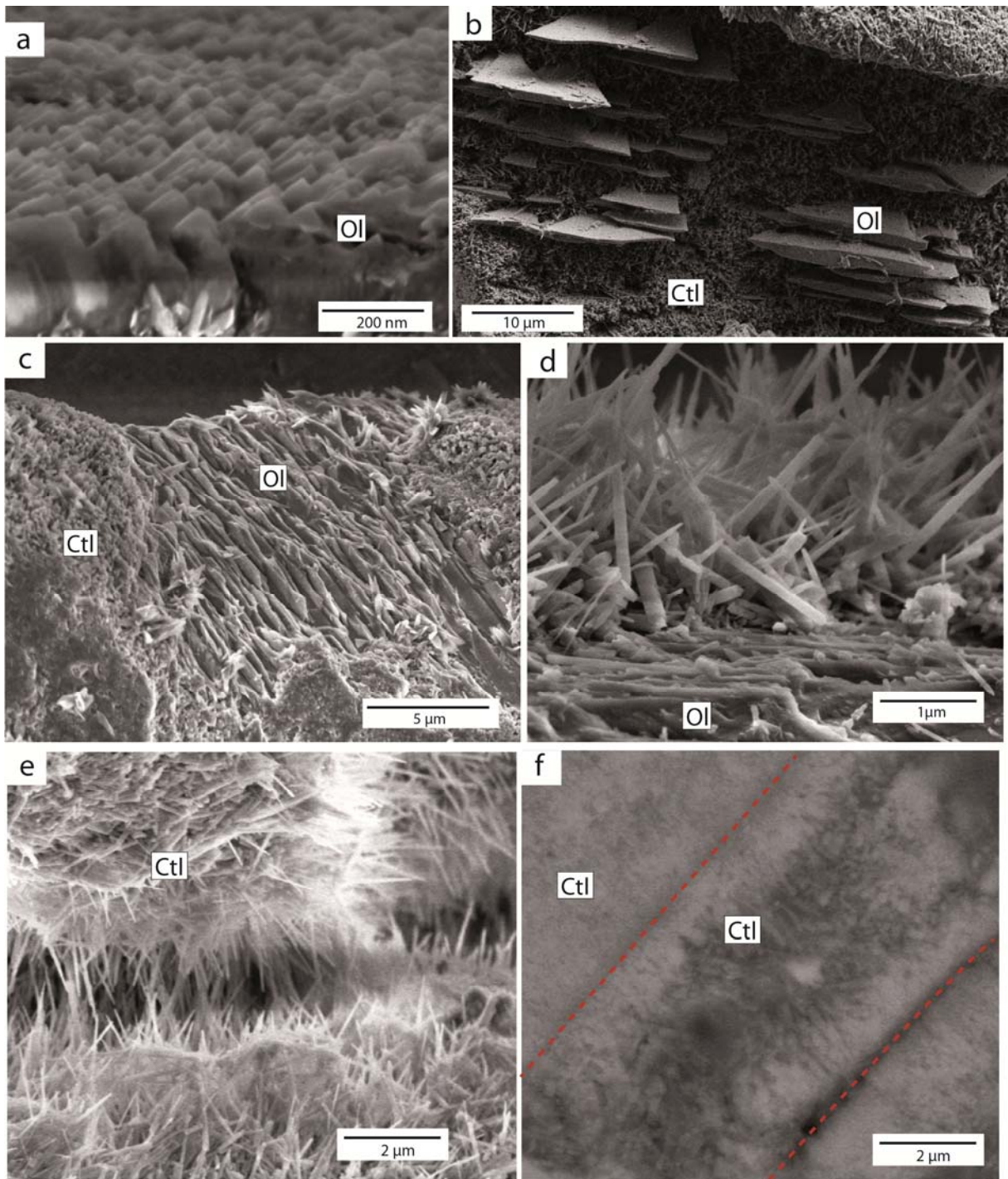




572

573

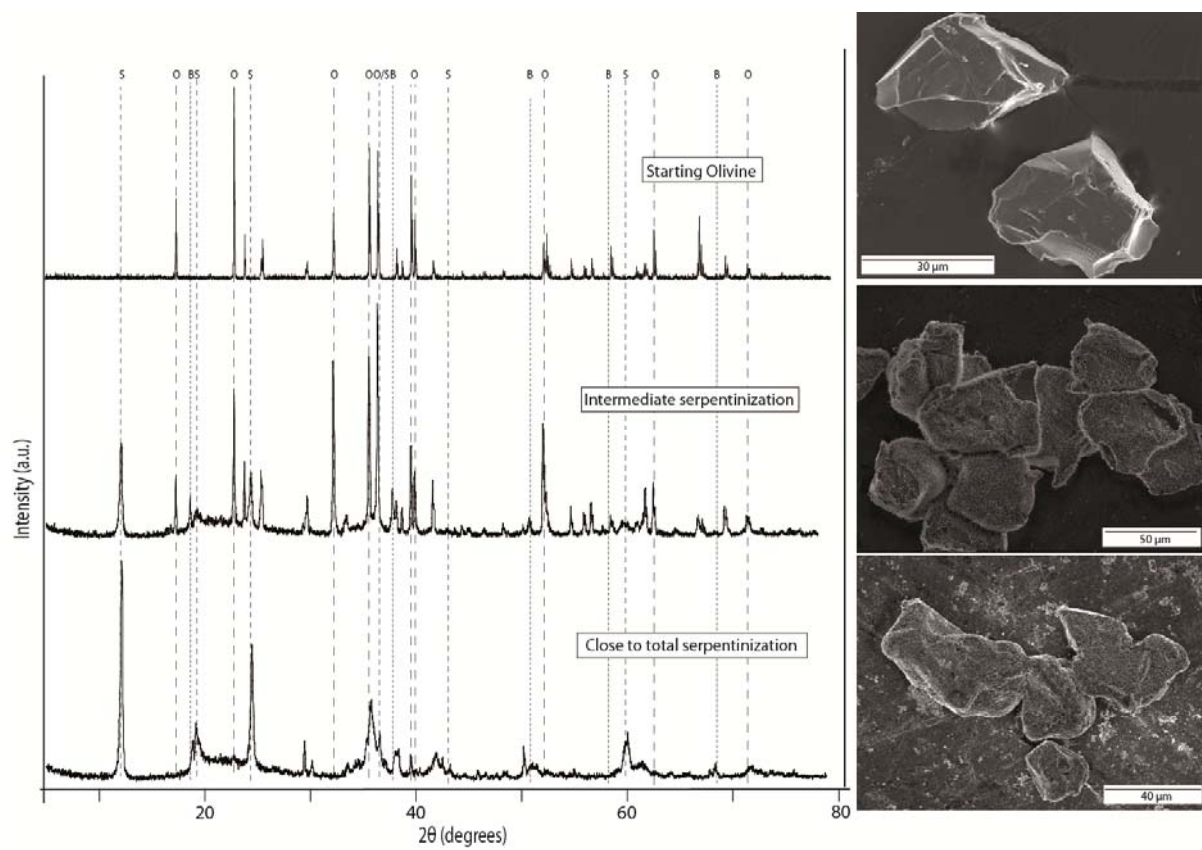
574 Figure 6
575



576
577

578

579 Figure 7



580

581

